PAPER

Check for updates

Interfacial electron-engineered tungsten oxynitride interconnected rhodium layer for highly efficient all-pH-value hydrogen production†

Ben Zhang,‡ Yijuan Zheng,‡ Zhenyu Xing, Zihe Wu, Chong Cheng, [ID] Tian Ma [ID] * and Shuang Li [ID] *

Designing and synthesizing eco-friendly and efficient catalysts for the hydrogen evolution reaction (HER) plays a crucial role in the field of large-scale and high-purity hydrogen production. However, it is severely hampered by the sluggish kinetics of the water dissociation step in non-acidic media. To optimize catalytic kinetics, interfacial electron engineering between active sites and supports has been regarded as an essential strategy to achieve compelling electrocatalytic all-pH-value-hydrogen production. Herein, we present the successful fabrication of WNO-coupled Rh layers (Rh–WNO) by a simple thermal treatment of a urea sol–gel with mixed W and Rh salts. This facile one-pot synthetic method is easy to scale up and the resulting Rh–WNO catalyst features Rh nanoclusters anchored on the surface of the well-ordered WNO crystals *via* Rh–N and Rh–O bonds. The optimal catalyst, Rh–WNO, delivered low overpotentials of 19, 22, and 134 mV at a current density of 10 mA cm^{-2} in 0.5 M H$_2$SO$_4$, 1.0 M KOH, and 1.0 M PBS, respectively. Notably, Rh–WNO exhibits a high turnover frequency (TOF) of 7.84 H$_2$ s^{-1} in alkaline conditions, which is much higher than those of Pt/C (0.9 H$_2$ s^{-1}), Rh/C (0.77 H$_2$ s^{-1}), and most of the reported HER electrocatalysts. This work may provide an effective and economic approach for scaling up the production of highly efficient and stable metal nitride-based HER catalysts.

1 Introduction

The growing urgent energy crisis and pollution problems have severely damaged the carbon balance of the earth, and the development of renewable energy has drawn widespread attention to solving these issues.[1–6] Hydrogen (H$_2$), as a promising alternative energy carrier for fossil fuels, offers great benefits for energy systems, including high gravimetric energy density, lower carbon emissions, and improved sustainability.[7–11] Electrocatalytic water splitting presents an ideal pathway to high-purity and large-scale hydrogen production.[12–16] However, the sluggish kinetics of the water dissociation step in non-acidic media severely hinder the practical applications of electrocatalytic hydrogen evolution.[17–20] Therefore, seeking efficient electrocatalysts to optimize hydrogen evolution reaction (HER) kinetics is crucial to achieving compelling HER activity. Modulation of the electronic structure of catalysts has been identified as a viable method for

designing highly efficient catalysts to overcome the effects of pH on water electrolysis.[21–25] Among various electronic structure modulation approaches, interfacial electron engineering of heterostructure electrocatalysts has been widely investigated, showing a variety of geometric, coordination, electronic, and synergistic effects.[25–28] Through the elaborate modulation of the interfacial electronic and geometric interactions, the adsorption and dissociation of H$_2$O molecules can be significantly enhanced, thus improving the HER activity over a wide range of pH.[25,29,30] Therefore, optimizing the interfacial electronic structure and establishing accurate structure–property relationships for the supported metal catalysts are the key points for improving their performance for HER.[19,31,32]

Based on the volcano curve of the calculated hydrogen adsorption energies, rhodium (Rh) has been considered as one of the most promising alternatives to Pt in HER.[33] Due to high intrinsic corrosion resistance to various media, Rh-based HER electrocatalysts are also available in all-pH-value electrolytes. However, since the intrinsic HER activity of Rh metal is 20–30 times lower than that of Pt metal, the performance of many reported Rh-based catalysts for HER is still far from satisfactory.[34] To enhance the activity of noble-metal-based catalysts, one popular strategy is to introduce suitable substrates.[35] The resulting synergistic and stable interface can modulate the

College of Polymer Science and Engineering, State Key Laboratory of Polymer Materials Engineering, Sichuan University, Chengdu 610065, China. E-mail: matian1991@scu.edu.cn; shuang.li@scu.edu.cn

† Electronic supplementary information (ESI) available. See DOI: https://doi.org/10.1039/d3ta06856k

‡ These authors contributed equally to this paper.

4484 | *J. Mater. Chem. A*, 2024, **12**, 4484–4491

This journal is © The Royal Society of Chemistry 2024

electronic structure of the active sites and the adsorption of intermediates to achieve enhancement of activity and stability.

Transition metal carbides (TMCs), nitrides (TMNs), and their mixtures, with precise crystal structures, are newly emerging catalysts support due to their earth abundance and superior stability especially the specific electronic interaction with supported noble metals.[36–38] As representative types, the molybdenum/tungsten carbides and nitrides have been discovered as promising supports for noble metals to facilitate the water-splitting process due to their unique surface electronic properties. For instance, WN with Pt-like electronic properties has been developed to tune the charge density of Ru, and optimize the interfacial Ru–H binding energy, thus greatly improving the HER performance.[39] The WC substrate can efficiently decrease the energy barriers of water dissociation, leading to significantly enhanced electrocatalytic activity of the lattice-confined atomic Pt in WC towards alkaline HER.[40] Recently, both theoretical and experimental studies have revealed that the surface-covered oxygen on TMN catalysts can optimize the binding energies of reaction intermediates, thus further enhancing their catalytic activity. For instance, the surface O and N provide efficient sites for coordinating other active metal atoms and offer great potential to manipulate the HER properties of supported metals.[41–44] The strong bonding between noble metal and O atoms highly improves the stability of supported metals, while metal–N species act as an active site for electrocatalysis.[25,42,45] Although incorporating O atoms into WN supports or N atoms into WO_x supports has a significant opportunity to manipulate the HER properties of supported noble metals, there is still a debate regarding the unclear structure information. Tungsten oxynitrides (WNO), which possess well-defined atom arrangements and crystal structures, can serve as an ideal platform to elucidate the role of N and O in terms of modulation of precise properties of noble metal atoms. Until now, the realization of controllable preparation of crystalline WNO has remained a great challenge due to its unique transitional phase, and the mechanism by which these interstitial N–O microenvironments affect the intrinsic hydrogen-evolving activities of the catalytic sites is also unclear. Therefore, it is a big deal to develop a green and highly efficient strategy to synthesize the distinctive WNO as a substrate for HER electrocatalyst.

Herein, we present the successful fabrication of WNO-coupled Rh layers (Rh–WNO) through a simple thermal treatment of a urea sol–gel with mixed W and Rh salts. This one-pot synthetic method is easy to scale up and the resulting Rh–WNO catalyst features Rh nanoclusters anchored on the surface of the well-ordered WNO crystals *via* Rh–N and Rh–O bonds. Owning to the unique electronic state and coordination environment of Rh layers, Rh–WNO exhibited significant activity enhancements in HER activity in wide pH. The optimized Rh–WNO catalyst requires overpotentials of only 19, 22, and 143 mV to reach the current density of 10 mA cm^{-2} in 0.5 M H_2SO_4, 1.0 M KOH, and 1.0 M phosphate buffer solution (PBS, pH = 7), respectively. Most importantly, Rh–WNO exhibits a high turnover frequency (TOF) of 7.84 H$_2$ s^{-1} under alkaline conditions, which is much higher than those of Pt/C (0.9 H$_2$ s^{-1}), Rh/C (0.77 H$_2$ s^{-1}), and

most of the reported HER electrocatalysts. The long-term stability over a wide range of pH further suggests its excellent HER performance.

2 Materials and methods

2.1 Materials

Ethanol (C_2H_5OH, 99.7%, Aladdin), rhodium(III) chloride hydrate ($RhCl_3 \cdot xH_2O$, 98%, Aladdin), tungsten(VI) chloride (WCl_6, 99%, Aladdin), urea (CH_4N_2O, 99.5%, Aladdin), platinum on carbon (Pt/C, 20%, Alfa Aesar), rhodium on carbon (Rh/C, 20%, Alfa Aesar), Nafion (D520, 5 wt%, Alfa Aesar), Ketjen black (KB), potassium hydroxide (KOH, 85%, Aladdin), PBS: sodium phosphate dibasic dihydrate ($Na_2HPO_4 \cdot 2H_2O$, 99.0%, Aladdin), and sodium dihydrogen phosphate monohydrate ($NaH_2PO_4 \cdot H_2O$, 99.0%, Aladdin) were used as received. Ultrapure water was used for the preparation of all aqueous solutions.

2.2 Synthesis

200 mg of WCl_6 and 10 mg of $RhCl_3 \cdot xH_2O$ powder were dispersed in ethanol (2 mL) to form a stable and transparent solution (Fig. S1†). 200 mg of urea was added to the above solution and stirred to dissolve. Then, 20 mg of KB was added, stirred for 30 min, and then transferred to a crucible for aging and complexation for 12 h to obtain a gel-like solid. The above operations were performed in the glove box. The gel was placed in a tube furnace in an Ar gas environment (flow rate 100 mL min^{-1}), and the temperature was increased to 70 °C at a heating rate of 1 °C min^{-1} and kept at a constant temperature for 2 h. After that, the temperature was increased to 600 °C at a heating rate of 5 °C min^{-1} and was held at that temperature for 3 h. Then, the sample was cooled to room temperature and passivated for 2 hours under the same argon flow. The obtained product was ground before use. Initial slow heating is important to avoid burst release of residual solvent. At a high temperature of 200 °C, urea is decomposed into NH$_2$, NH$_3$, HNCO, and H$_2$NCO groups to participate in the nitridation reaction. To analyze the effect of pyrolysis temperature on HER performance, the solid powders were pyrolyzed at 500, 700, 800, and 900 °C for 3 h (denoted as Rh–W-500, Rh–W-700, Rh–W-800, and Rh–W-900). The preparation process of WNO is the same as that of Rh–WNO, except that $RhCl_3 \cdot xH_2O$ is not added to the solution.

2.3 Characteristic measurements

Scanning electron microscopy (SEM) images were obtained using a Thermo Fisher Scientific (FEI) Apreo S HiVoc. The coating of gold was deposited at a layer thickness of 1 nm. The transmission electron microscopy (TEM) was performed using a Tecnai G2 F20 S-TWIN instrument operated at 200 kV. The aberration-corrected high-angle annular darkfield scanning transmission electron microscopy (AC HAADF-STEM) was performed on a JEOL JEM-ARM 200F scanning transmission electron microscope equipped with a cold field emission electron source and DCOR probe corrector (CEOS GmbH), 100 mm^2

This journal is © The Royal Society of Chemistry 2024

J. Mater. Chem. A, 2024, 12, 4484–4491 | 4485

JEOL Centurio EDX detector, and Gatan GIF Quantum ERS electron energy-loss spectrometer operated at 200 kV. X-ray diffraction (XRD) measurements were performed on a Rigaku Ultima IV with Cu Kα irradiation. X-ray photoelectron spectra (XPS) measurements were performed on a K-Alpha™+ X-ray photoelectron spectrometer system (Thermo Scientific) using a hemispheric 180° dual-focus analyzer with 128-channel detector and a monochromatic Al Kα irradiation. X-ray absorption spectra (XAS) were collected on the beamline BL07A1 in NSRRC (National Center for Synchrotron Radiation Research). The X-ray radiation is monochromatized by scanning a Si (111) double-crystal monochromator.

3 Results and discussion

3.1 Synthesis and morphological characterizations

The Rh–WNO was synthesized *via* a facile one-pot approach (Fig. 1). Initially, a solid sol was created by mixing rhodium chloride, tungsten chloride, and urea in ethanol, which resulted in the formation of a precursor for the following nitridation step (Table S1†). During the pyrolysis process, tungsten sources in the gel-like precursor reacted with the highly reactive N and O atoms in urea to form a WNO substrate. At the same time, rhodium ions were reduced to metallic Rh by reducing substances dissociated through urea calcination and anchored onto WNO *via* Rh–N or Rh–O bonds. Urea served as both a complexing agent and nitrogen source, playing a critical role in preventing the agglomeration of Rh species. This greatly improved the utilization of Rh sites and the mass activity of the composite catalysts. For comparison, Rh–WO$_3$ featuring only Rh–O bonds was prepared *via* an identical process but without urea to evaluate the importance of N/O coordination in HER. Additionally, pristine WNO and samples with different Rh contents and various heat treatment temperatures were synthesized by a similar approach (as shown in Table S1†).

The local structure of Rh–WNO was initially analyzed by TEM (Fig. 2 and S2†). As shown in Fig. 2a the metal composite and carbon layer formed an interconnected nanohybrid structure. The unique morphology of Rh–WNO was further examined using high-angle annular dark-field scanning TEM (HAADF-STEM). It can be observed that the WNO crystal structures are discontinuous, indicating that the Rh species and WNO matrix are interpenetrating and cross-linked with each other, which

could enhance the support effects and therefore benefit the electrocatalysis process (Fig. 2b and c). The atomic-resolution STEM image revealed that WNO is surrounded by a slightly darker atomic arrangement of Rh nanoclusters (Fig. 2d and e). Fig. 2f shows the typical Rh and WNO interface regions, where the well-connected crystal boundary further confirms the strong interaction between the Rh clusters and the WNO matrix. It is observed that the Rh clusters were mostly anchored on the WNO (111) lattice. Specifically, N- and O-terminated WNO (111) can provide a large number of anchoring sites, thereby facilitating the formation of interfacial Rh–N and Rh–O, and obtaining stable Rh clusters on the WNO substrate. Based on the above structure information, we proposed a structured scheme for the Rh–WNO catalyst with a well-connected two-crystal structure by Rh–N and Rh–O bond (Fig. 2g). EDX elemental mapping was further conducted to confirm the existence of Rh in the as-synthesized catalyst (Fig. 2h, S3 and S4†). The homogeneous distribution of W, N, and O elements again verified the successful formation of WNO nanocrystalline. More importantly, Rh is mainly distributed along with the W, N, and O elements, indicating that the Rh layers are uniformly anchored on the WNO nanonetworks.

3.2 Understanding of the electronic interaction

The crystal structure of Rh–WNO was investigated by the powder XRD technique. As shown in Fig. 3a, the diffraction peaks of Rh–WNO at 37.6°, 43.7°, 63.5°, and 76.2°, belonged to the characteristic (111), (200), (220), and (311) lattice planes of W$_{0.62}$(N$_{0.62}$O$_{0.38}$) (JCPDF no. 25-1254), confirming the formation of face-centered cubic WNO nanocrystalline. It is also reasonable to believe that the mainly exposed surface of Rh–WNO is the WNO (111) surface, consistent with HAADF-STEM images. No obvious Rh or RhO$_x$ peaks can be observed in the XRD pattern, verifying the uniform dispersion of Rh species with ultra-fine cluster size, which is consistent with the results of TEM. The broad peak observed at about 24° belongs to the typical diffraction of the carbon matrix. In contrast, when the composite precursor was carbonized under the same condition without adding urea, Rh–WO$_3$ was obtained. The XRD result of Rh–WO$_3$ revealed the characteristic peaks of WO$_3$ (JCPDF no. 46-1096) and metallic Rh particles (JCPDF no. 05-0685), indicating that urea not only provided N species but also acted as
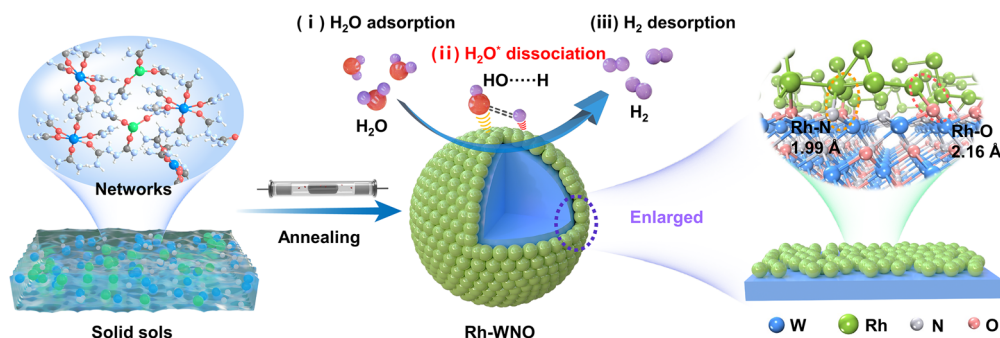

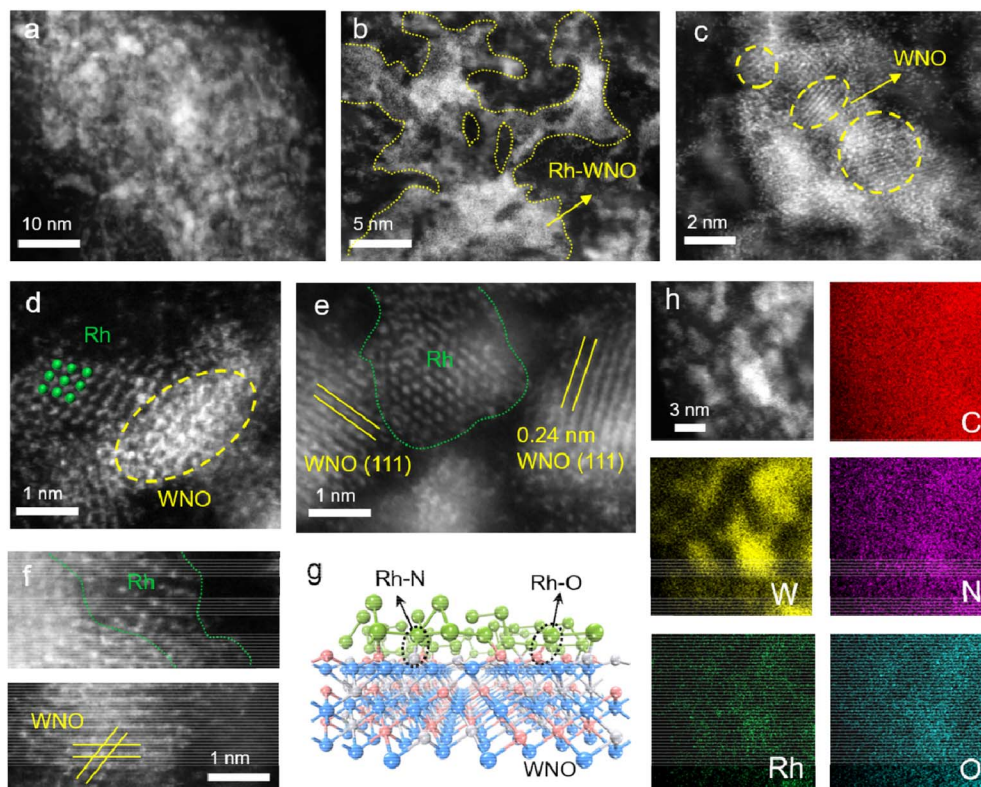Fig. 1 Schematic illustration of the Rh–WNO catalyst with Rh layers coupled on WNO nanoparticles.

4486 | *J. Mater. Chem. A*, 2024, **12**, 4484–4491

This journal is © The Royal Society of Chemistry 2024

Fig. 2 Morphological characterizations of Rh–WNO. (a) Dark-field TEM images of Rh–WNO. (b–e) HAADF-STEM images of Rh–WNO at different magnifications. (f) The region with typical Rh and WNO lattices. (g) The structural model of Rh–WNO. (h) EDX elemental mapping of Rh–WNO.

a dispersion agent to prevent the formation of large Rh particles (Fig. S5†).

To gain insights into the chemical composition and bonding structure, XPS measurements were performed (Fig. S6†). The XPS results confirmed that the as-synthesized catalyst consisted of Rh (2.58 wt%, 0.53 at%), C (40.97 wt%, 72.13 at%), W (40.92 wt%, 6.07 at%), N (2.23 wt%, 3.93 at%), and O (13.30 wt%, 17.33 at%) elements. The Rh 3p spectrum of Rh–WNO can be divided into two doublet peaks, corresponding to metallic (307.77 eV and 312.37 eV) and oxidized Rh (309.70 eV and 314.30 eV) species, indicating a partial reduction of Rh^{3+} to Rh^0 *via* the annealing treatment (Fig. 3b and S7†).[46] Compared to the bonding energy of Rh^{3+} in Rh/C, the peak of Rh–WNO is positively shifted by ≈ 0.15 eV, suggesting the electron transfer from Rh species to the internal WNO substrate. The high-resolution W 4f spectrum of Rh–WNO shows four peaks that can be fitted into two pairs of 32.72, 34.79 eV and 35.72, 37.87 eV (Fig. S7b†), which belong to W–N and W–O bonds, respectively.[47] The simultaneous presence of W–N and W–O bonds confirmed the formation of WNO species. Upon comparing the high-resolution W 4f spectra of Rh–WNO with pristine WNO, a negative shift was observed, suggesting a significant electron donation from Rh nanoclusters and WNO owing to the considerably stronger electronegativity of W compared to Rh.[48] The N 1s spectra showed a typical peak at ∼397.38 eV (Fig. 3c), which can be assigned to the metal–N bond, further verifying

the presence of W–N bonds. In addition, peaks at 398.4, 399.82, 401.08, and 402.11 eV belonged to pyridinic N, pyrrolic N, graphitic N, and oxidized N, respectively, indicating the doping of heteroatom N in carbon.[49] As shown in the O 1s spectrum of Rh–WNO (Fig. S8†), peaks at 530.87 and 531.65 eV are attributed to the metal–O bond and adsorbed O. Based on the XPS results discussed above, the interfacial electron interaction between the Rh nanoclusters and WNO substrate may induce the local electron redistribution, thereby regulating the adsorption energy of HER intermediate and promoting improved catalytic performance.[50]

To further investigate the local electronic structure and coordination environments of Rh atoms, XAS spectroscopy measurements were performed at the Rh K-edge. The normalized X-ray absorption near edge structure (XANES) spectra for the Rh K-edge of Rh–WNO and standard samples are presented in Fig. 3d. In comparison to Rh foil, RhO, and Rh_2O_3 standard reference samples, the absorption edge of Rh K-edge for Rh–WNO exhibited a positive shift than Rh foil and RhO, but lower than Rh_2O_3. The result manifests an average Rh valence between +2 and +3, which is consistent with the XPS results. The extended X-ray absorption fine structure (EXAFS) spectra of Rh–WNO showed peaks at approximately 1.5 Å and 1.8 Å, which can be ascribed to the scattering paths of Rh–N and Rh–O coordination, respectively, thus validating the presence of Rh–O and Rh–N interfacial bonds between Rh layers and the WNO
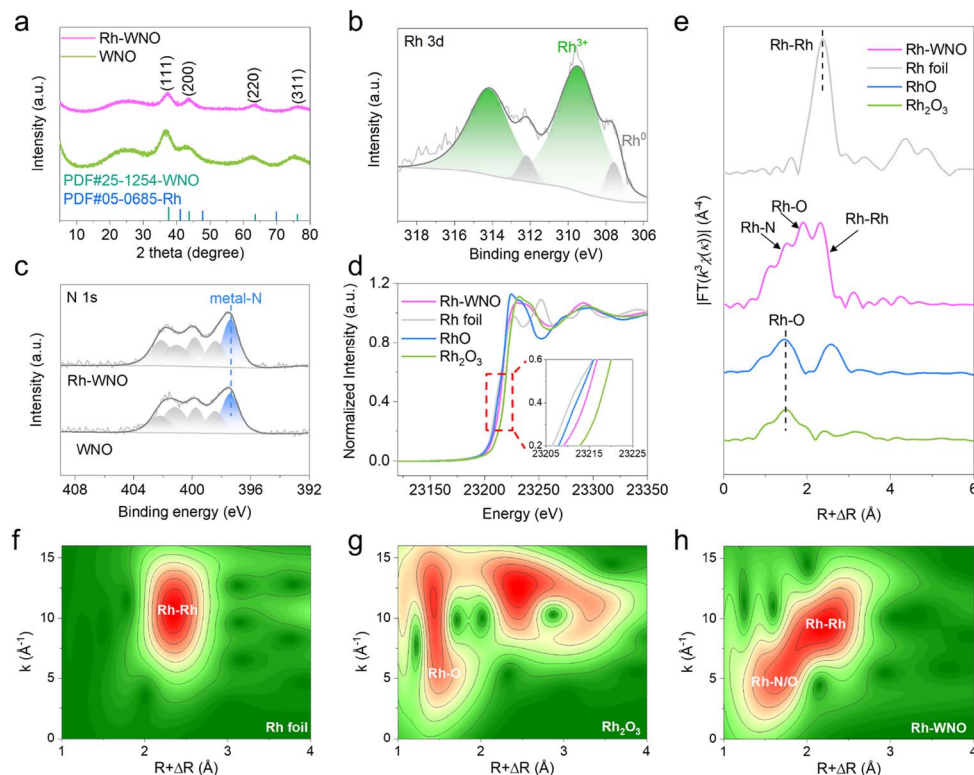
This journal is © The Royal Society of Chemistry 2024

J. Mater. Chem. A, 2024, **12**, 4484–4491 | **4487**

Fig. 3 Structural characterizations of Rh−WNO. (a) XRD patterns of Rh−WNO and WNO. XPS spectra of (b) Rh 3d and (c) N 1s. (d) Rh K-edge XANES spectra. (e) Fourier-transformed k^3-weighted EXAFS spectra of Rh−WNO and standard samples. (f−h) WT analysis at the Rh K-edge of different samples.
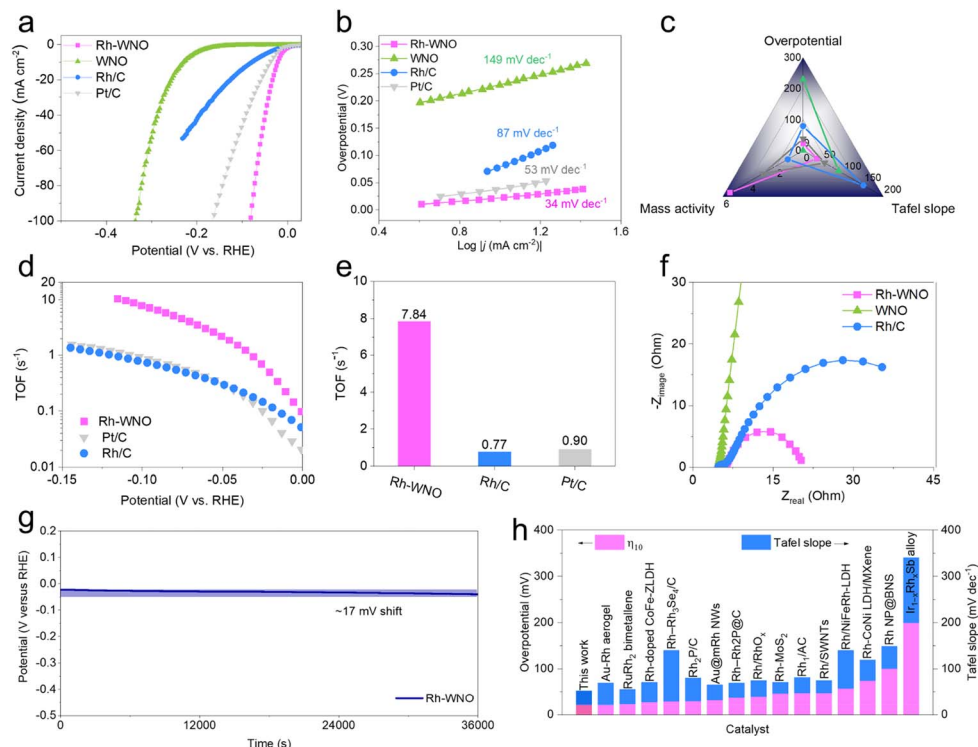
substrate (Fig. 3e). The Rh–O bond lengths in Rh–WNO differ from the Rh–O bonds in Rh_2O_3 due to spatial effects in the atomic arrangement at the interface between clusters and substrate.[51] Notably, the significant difference in the bond lengths between Rh–N and Rh–O may arise from the different atomic arrangements of N, and O elements in nanocrystalline WNO, in line with the postulated structure of WNO-coupled Rh layers. The peak at approximately 2.3 Å refers to the Rh–Rh bond in metallic Rh, suggesting the clustering of Rh elements. Consistent results were obtained from the wavelet transform (WT) analyses of the Rh K-edge data (Fig. 3f–h).[52] The maximum intensity value at $k \approx 9.8$ Å^{-1} ascribed to Rh–Rh backscattering contributions was detected, with a negative shift compared to that of Rh foil (10.5 Å^{-1}), indicating the absence of Rh–W scattering. The weaker WT signal at $k \approx 4.8$ Å^{-1} reveals the formation of Rh–O/N. The XANES and EXAFS results together with the XPS results reveal that Rh–WNO has a unique interstitial N and O microenvironments between Rh nanoclusters and the WNO substrate, and exhibits a core–shell-like structure.

3.3 Electrocatalytic activity toward HER

As a proof-of-concept application, the electrocatalytic HER performance of Rh–WNO was assessed in Ar-saturated 1.0 M KOH. Considering the cost and activity, Rh–WNO with the optimal Rh loading (2.58 wt% Rh by 10 mg Rh feeding) was selected as the representative sample (Fig. S9†). The commercial Pt/C (20 wt% Pt) and Rh/C (10 wt% Rh) were used as

reference catalysts for comparison. Fig. 4a presents the linear sweep voltammetry (LSV) curves of Rh–WNO, Rh/C, WNO, and Pt/C obtained at a scan rate of 10 mV s^{-1}; where Rh–WNO exhibited significantly higher HER activity than Rh/C and Pt/C. Specifically, at the current density of 10 mA cm^{-2}, Rh–WNO required the lowest overpotential of 22 mV, which is superior to those of WNO (229 mV), Rh/C (79 mV), and Pt/C (38 mV) (Fig. 4a and S10†). Moreover, Rh–WO₃, which is synthesized without urea, exhibits a high overpotential of 83 mV at the current density of 10 mA cm^{-2}, again indicating that the Rh–N species acted as an active site for HER. Tafel slopes were calculated to further analyze the HER kinetics of the catalysts. As shown in Fig. 4b, the Rh–WNO obtained the lowest Tafel slopes of 34.7 mV dec^{-1}, which is outperforming that of Rh/C (150 mV dec^{-1}) and Pt/C (88 mV dec^{-1}). The exchange current densities (j_0) were measured to evaluate the intrinsic activity of the catalysts (Fig. S11†). The Rh–WNO achieved the highest value of 1.547 mA cm^{-2} compared with WNO (0.199 mA cm^{-2}), Rh/C (1.478 mA cm^{-2}) and Pt/C (1.319 mA cm^{-2}), also verifying the high intrinsic activity of Rh–WNO. As shown in Fig. 4c, the Rh–WNO catalyst presents the highest mass activity of 5.47 A mg^{-1} at an overpotential of 100 mV, which is also superior to that of 20% Pt/C (3.00 A mg^{-1}) and 10% Rh/C (1.14 A mg^{-1}). Meanwhile, Rh–WNO exhibited a turnover frequency (TOF) of 7.84 H₂ s^{-1}, which is more than 8 times and 10 times higher than those of Pt/C (0.9 H₂ s^{-1}) and Rh/C (0.77 H₂ s^{-1}), respectively, and also exceeded those of some recently reported HER electrocatalysts

4488 | *J. Mater. Chem. A*, 2024, **12**, 4484–4491

This journal is © The Royal Society of Chemistry 2024

Fig. 4 Electrocatalytic HER performance in 1.0 M KOH. (a) LSV curves and (b) Tafel plots of different catalysts in 1.0 M KOH. (b) Comparison of Tafel slopes, overpotentials at 10 mA cm^{-2}, and normalized current densities based on mass at the overpotential of 100 mV. (c) Overall evaluation of the properties of Rh–WNO. (d) TOF plots and (e) TOF values of Rh–WNO, Rh/C, and Pt/C at the overpotential of 100 mV. (f) Nyquist plots of Rh–WNO, Rh/C, and Pt/C. (g) Longtime stability of Rh–WNO for HER a–t 10 mA cm^{-2}. (h) Comparison of overpotentials at the current density of 10 mA cm^{-2} and Tafel slope for Rh–WNO with other reported Rh-based catalysts.

at the overpotential of 100 mV (Fig. 4d and e).[33] The electrochemical impedance spectroscopy (EIS) plots indicated the fastest electron transfer during HER of Rh–WNO (Fig. 4f). The electrochemical surface areas (ECSA) were further assessed by the typical cyclic voltammetry (CV) method. The electrochemical double-layer capacitance (C_{dl}) of Rh–WNO was measured to be 4.3 mF cm^{-2}, which is smaller than that of Rh/C (5.1 mF cm^{-2}) but much greater than that of WNO (2.7 mF cm^{-2}), proving that more catalytically active sites were exposed (Fig. S12†). The stability test of Rh–WNO exhibited a negligible overpotential decline after 10 hours of HER at the current density of 10 mA cm^{-2} (Fig. 4g), indicating the good electrochemical durability of Rh–WNO. Notably, the performance of Rh–WNO is comparable to those of previously reported state-of-the-art electrocatalysts (Fig. 4h and Table S2†). Commercial Rh/C exhibited worse HER performance than Pt/C in all-pH conditions, confirming that the metallic Rh sites on a carbon substrate are much inferior to Pt sites towards HER. The interfacial electron engineering strategy effectively promoted the electron transfer from Rh to WNO in Rh–WNO, thus the obtained Rh sites with positive charges exhibited optimal adsorption of *H and water. Moreover, the polarized Rh–N and Rh–O bonds favor the H–OH cleavage of polarized H$_2$O molecules, which is crucial for HER in alkaline media.[53,54] To further explore the role of each component of the Rh-doped WNO composite catalyst in catalyzing the HER reaction, Rh–

H$_{0.33}$WO$_3$, Rh–WNO, Rh–WCO/W, Rh–WCO, and Rh–W$_2$C/WN were synthesized under the calcination temperature of 500 °C, 600 °C, 700 °C, 800 °C, and 900 °C, respectively, which were characterized and tested to further investigate the influence of the heat treatment temperature (Fig. S13 and S14†). According to XRD results shown in Fig. S13,† H$_{0.33}$WO$_3$ mainly exists in Rh–H$_{0.33}$WO$_3$ and a mixture state of WCO/W is obtained in Rh–WCO/W. When the temperature is further increased to 800 °C, WCO substrate is obtained (Rh–WCO) and all W species in the samples at 900 °C are converted to WN or W$_2$C (Rh–WN/W$_2$C). The optimal calcination temperature is 600 °C, and that is the temperature to obtain Rh–WNO. These HER performances of catalysts with different substrates suggested that the unique interstitial O and N microenvironment active synergistic interaction between WNO nanonetworks and coupled Rh nanoclusters could enhance HER activity, therefore providing the possibility for further designing of efficient HER catalysts.

For the practical application of hydrogen production, electrocatalysts need to work efficiently and stably under a wide range of conditions. Consequently, seeking pH-universal HER catalysts with optimal activity is of great importance but still challenging. To reveal the pH universality of Rh–WNO interconnected nanohybrid structure for catalyzing HER, the electrocatalytic performances in 0.5 M H$_2$SO$_4$ and 1.0 M PBS were further investigated. As shown in Fig. 5, the overpotentials of Rh–WNO at 10 mA cm^{-2} in 0.5 M H$_2$SO$_4$ solution and 1.0 M PBS
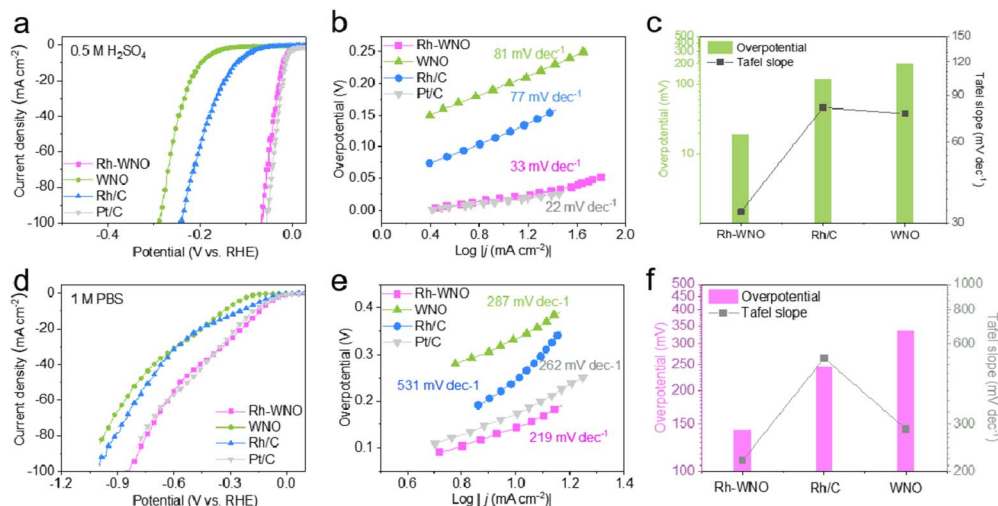
Fig. 5 Electrocatalytic HER performance of the catalysts in acidic and neutral electrolytes. (a and d) LSV plots, (b and e) Tafel plots, (c and f) overpotentials at 10 mA cm^{-2} and Tafel slope of Rh−WNO and compared samples in 0.5 M H$_2$SO$_4$ (a−c) and 1 M PBS (d−f).

solution were 19 mV and 143 mV, respectively. In the acidic and neutral conditions, Rh−WNO showed Tafel slopes of 33 mV dec^{-1} and 219 mV dec^{-1}, respectively, which are comparable to those of Rh/C (77 mV dec^{-1}, 531 mV dec^{-1}) and Pt/C (22 mV dec^{-1}, 262 mV dec^{-1}). Notably, the HER activity gap of Rh−WNO ($\Delta\eta_{10} = 2$ mV) between acidic and alkaline media is narrower compared with those of Rh/C ($\Delta\eta_{10} = 41$ mV) and Pt/C ($\Delta\eta_{10} = 24$ mV), indicating that Rh−WNO can well overcome the water dissociation energy barrier (Fig. S15†).

Based on the above results, the obtained Rh−WNO catalyst demonstrates enhanced activity in all-pH value, benefiting from the interfacial synergetic effect. In acidic conditions, Rh−WNO shows Pt/C-like catalytic activity, which is attributed to the optimized *H adsorption on positive Rh sites. In alkaline media, the positively charged Rh sites and the negatively charged WNO substrate in Rh−WNO facilitated the H−OH cleavage, thus overcoming the water dissociation energy barrier. Whereas Pt/C suffers from the sluggish reaction kinetics due to the water dissociation process. As for neutral electrolytes, the lack of H$^+$ and OH$^-$, and the rigidity of the interfacial water layer hinder the diffusion of intermediates,[55] leading to relatively poor catalytic efficiency of Rh−WNO, nevertheless, which was still comparable to that of Pt/C.

4 Conclusion

In conclusion, we have successfully developed a one-pot synthetic method for WNO-coupled Rh nanocluster electro-catalyst for all-pH-value hydrogen production. The Rh−WNO catalyst features Rh nanoclusters anchored on the surface of well-ordered WNO crystals via Rh−N and Rh−O bonds, and the interfacial bonding might promote the electronic interaction between the substrate and Rh layers. As a consequence, the resulting Rh−WNO exhibited significant activity enhancements in wide pH HER, requiring overpotentials of 19, 22, and 143 mV to reach the current density of 10 mA cm^{-2} in 0.5 M H$_2$SO$_4$,

1.0 M KOH, and 1.0 M PBS, respectively. Notably, Rh−WNO exhibits a high turnover frequency (TOF) of 7.84 H$_2$ s^{-1} in alkaline conditions, which is much higher than those of Pt/C (0.9 H$_2$ s^{-1}), Rh/C (0.77 H$_2$ s^{-1}), and most of the reported HER electrocatalysts. This work may offer a promising approach towards the scaling up of the fabrication of robust and efficient metal nitride-based HER catalysts.

Conflicts of interest

The authors declare no conflict of interest.

Acknowledgements

References

1 J. Deng, J. A. Iñiguez and C. Liu, *Joule*, 2018, **2**, 846–856.
2 M. Dunwell, W. Luc, Y. Yan, F. Jiao and B. Xu, *ACS Catal.*, 2018, **8**, 8121–8129.
3 Y. Jiao, Y. Zheng, M. Jaroniec and S. Z. Qiao, *Chem. Soc. Rev.*, 2015, **44**, 2060–2086.
4 C. J. Van der Ham, M. T. Koper and D. G. Hetterscheid, *Chem. Soc. Rev.*, 2014, **43**, 5183–5191.
5 K. P. Kuhl, T. Hatsukade, E. R. Cave, D. N. Abram, J. Kibsgaard and T. F. Jaramillo, *J. Am. Chem. Soc.*, 2014, **136**, 14107–14113.

4490 | *J. Mater. Chem. A*, 2024, **12**, 4484–4491

This journal is © The Royal Society of Chemistry 2024

6 X. Li and J. Wang, *InfoMat*, 2020, **2**, 3–32.

7 X. Zou and Y. Zhang, *Chem. Soc. Rev.*, 2015, **44**, 5148–5180.

8 H. Su, H. Lou, Z. Zhao, L. Zhou, Y. Pang, H. Xie, C. Rao, D. Yang and X. Qiu, *Chem. Eng. J.*, 2022, **430**, 132770.

9 W. Kang, Y. Feng, Z. Li, W. Yang, C. Cheng, Z. Z. Shi, P. Yin, G. Shen, J. Yang and C. Dong, *Adv. Funct. Mater.*, 2022, **32**, 2112367.

10 Q. Liu, B. Lu, F. Nichols, J. Ko, R. Mercado, F. Bridges and S. Chen, *SusMat*, 2022, **2**, 335–346.

11 Z. Wu, J. Yang, W. Shao, M. Cheng, X. Luo, M. Zhou, S. Li, T. Ma, C. Cheng and C. Zhao, *Adv. Fiber Mater.*, 2022, **4**, 774–785.

12 Y. Zhao, H. Cong, P. Li, D. Wu, S. Chen and W. Luo, *Angew. Chem., Int. Ed.*, 2021, **60**, 7013–7017.

13 J. Li, H. Yoon, T. Oh and E. D. Wachsman, *Appl. Catal., B*, 2009, **92**, 234–239.

14 Y. Oh, H. Roh, K. Jun and Y. Baek, *Int. J. Hydrogen Energy*, 2003, **28**, 1387–1392.

15 A. Antzara, E. Heracleous and A. A. Lemonidou, *Appl. Energy*, 2016, **180**, 457–471.

16 K. Xu, H. Ding, M. Zhang, M. Chen, Z. Hao, L. Zhang, C. Wu and Y. Xie, *Adv. Mater.*, 2017, **29**, 1606980.

17 J. Zhang, L. Zhang, J. Liu, C. Zhong, Y. Tu, P. Li, L. Du, S. Chen and Z. Cui, *Nat. Commun.*, 2022, **13**, 5497.

18 Z. Zhu, J. Hao, H. Zhu, S. Sun, F. Duan, S. Lu and M. Du, *Adv. Fiber Mater.*, 2021, **3**, 117–127.

19 L.-F. Gu, J.-J. Chen, T. Zhou, X.-F. Lu and G.-R. Li, *Nanoscale*, 2020, **12**, 11201–11208.

20 S. L. Zhang, X. F. Lu, Z.-P. Wu, D. Luan and X. W. Lou, *Angew. Chem., Int. Ed.*, 2021, **60**, 19068–19073.

21 B. Zhou, R. Gao, J. J. Zou and H. Yang, *Small*, 2022, **18**, 2202336.

22 L. Chen, X. Guo, R. Shao, Q. Yan, L. Zhang, Q. Li and H. Liang, *Nano Energy*, 2021, **81**, 105636.

23 C. Cai, K. Liu, L. Zhang, F. Li, Y. Tan, P. Li, Y. Wang, M. Wang, Z. Feng, D. M. Meira, W. Qu, A. Stefancu, W. Li, H. Li, J. Fu, H. Wang, D. Zhang, E. Cortes and M. Liu, *Angew. Chem., Int. Ed.*, 2023, **62**, e202300873.

24 S. Xiao, Y. Zheng, X. Wu, M. Zhou, X. Rong, L. Wang, Y. Tang, X. Liu, L. Qiu and C. Cheng, *Small*, 2022, **18**, 2203281.

25 X. Wu, S. Xiao, Y. Long, T. Ma, W. Shao, S. Cao, X. Xiang, L. Ma, L. Qiu, C. Cheng and C. Zhao, *Small*, 2022, **18**, 2105831.

26 J. Yang, Y. Shen, Y. Sun, J. Xian, Y. Long and G. Li, *Angew. Chem., Int. Ed.*, 2023, **62**, e202302220.

27 D. Wang, Q. Li, C. Han, Q. Lu, Z. Xing and X. Yang, *Nat. Commun.*, 2019, **10**, 3899.

28 Y. Wu, Y. Li, J. Gao and Q. Zhang, *SusMat*, 2021, **1**, 66–87.

29 J. Zhang, G. Chen, Q. Liu, C. Fan, D. Sun, Y. Tang, H. Sun and X. Feng, *Angew. Chem., Int. Ed.*, 2022, **61**, e202209486.

30 F. Li, G. Han, H. Noh, I. Ahmad, I. Jeon and J. Baek, *Adv. Mater.*, 2018, **30**, 1803676.

31 C. Yang, Z. Wu, Z. Zhao, Y. Gao, T. Ma, X. Luo, C. Cheng, Y. Wang, S. Li and C. Zhao, *Adv. Mater.*, 2023, 2303331, DOI: **10.1002/adma.202303331**.

32 F. Zhang, J. Chen and J. Yang, *Adv. Fiber Mater.*, 2022, **4**, 720–735.

33 K. Chen, Z. Wang, L. Wang, X. Wu, B. Hu, Z. Liu and M. Wu, *Nano-Micro Lett.*, 2021, **13**, 2100662y.

34 M. K. Kundu, R. Mishra, T. Bhowmik and S. Barman, *J. Mater. Chem. A*, 2018, **6**, 23531–23541.

35 X. Ma, H. Xiao, Y. Gao, M. Zhao, L. Zhang, J. Zhang, J. Jia and H. Wu, *J. Mater. Chem. A*, 2023, **11**, 3524–3534.

36 S. Jing, J. Lu, G. Yu, S. Yin, L. Luo, Z. Zhang, Y. Ma, W. Chen and P. K. Shen, *Adv. Mater.*, 2018, **30**, 1705979.

37 J. Diao, Y. Qiu, S. Liu, W. Wang, K. Chen, H. Li, W. Yuan, Y. Qu and X. Guo, *Adv. Mater.*, 2020, **32**, 1905679.

38 M. Zeng, Y. Chen, J. Li, H. Xue, R. G. Mendes, J. Liu, T. Zhang, M. H. Rümmeli and L. Fu, *Nano Energy*, 2017, **33**, 356–362.

39 G. Liu, J. Zhang, H. Ren, Y. Tang and H. Sun, *Mater. Chem. Front.*, 2023, **7**, 4100–4108.

40 T. Ma, H. Cao, S. Li, S. Cao, Z. Zhao, Z. Wu, R. Yan, C. Yang, Y. Wang, P. A. van Aken, L. Qiu, Y. Wang and C. Cheng, *Adv. Mater.*, 2022, **34**, 2206368.

41 Y. Yang, Y. Qian, H. Li, Z. Zhang, Y. Mu, D. Do, B. Zhou, J. Dong, W. Yan and Y. Qin, *Sci. Adv.*, 2020, **6**, eaba6586.

42 X. Cheng, Y. Lu, L. Zheng, Y. Cui, M. Niibe, T. Tokushima, H. Li, Y. Zhang, G. Chen and S. Sun, *Nano Energy*, 2020, **73**, 104739.

43 X. Wang, Z. Chen, X. Zhao, T. Yao, W. Chen, R. You, C. Zhao, G. Wu, J. Wang and W. Huang, *Angew. Chem., Int. Ed.*, 2018, **130**, 1962–1966.

44 M. Cao, K. Liu, Y. Song, C. Ma, Y. Lin, H. Li, K. Chen, J. Fu, H. Li, J. Luo, Y. Zhang, X. Zheng, J. Hu and M. Liu, *J. Energy Chem.*, 2022, **72**, 125–132.

45 W. Zang, T. Sun, T. Yang, S. Xi, M. Waqar, Z. Kou, Z. Lyu, Y. P. Feng, J. Wang and S. J. Pennycook, *Adv. Mater.*, 2021, **33**, 2003846.

46 W. Wang, W. Geng, L. Zhang, Z. Zhao, Z. Zhang, T. Ma, C. Cheng, X. Liu, Y. Zhang and S. Li, *Small*, 2023, **19**, 2206808.

47 S. Qin, Y. Duan, X. L. Zhang, L. R. Zheng, F. Y. Gao, P. P. Yang, Z. Z. Niu, R. Liu, Y. Yang, X. S. Zheng, J. F. Zhu and M. R. Gao, *Nat. Commun.*, 2021, **12**, 2686.

48 G. Meng, H. Tian, L. Peng, Z. Ma, Y. Chen, C. Chen, Z. Chang, X. Cui and J. Shi, *Nano Energy*, 2021, **80**, 105531.

49 S. Cao, Z. Zhao, Y. Zheng, Z. Wu, T. Ma, B. Zhu, C. Yang, X. Xiang, L. Ma and X. Han, *Adv. Mater.*, 2022, **34**, 2200255.

50 H. Liang, S. Bruller, R. Dong, J. Zhang, X. Feng and K. Mullen, *Nat. Commun.*, 2015, **6**, 7992.

51 K. Zheng, Y. Li, B. Liu, F. Jiang, Y. Xu and X. Liu, *Angew. Chem., Int. Ed.*, 2022, **61**, e202210991.

52 H. Funke, A. Scheinost and M. Chukalina, *Phys. Rev. B: Condens. Matter Mater. Phys.*, 2005, **71**, 094110.

53 C. Cai, K. Liu, Y. Zhu, P. Li, Q. Wang, B. Liu, S. Chen, H. Li, L. Zhu, H. Li, J. Fu, Y. Chen, E. Pensa, J. Hu, Y.-R. Lu, T.-S. Chan, E. Cortes and M. Liu, *Angew. Chem., Int. Ed.*, 2022, **61**, e202113664.

54 H. Li, K. Liu, J. Fu, K. Chen, K. Yang, Y. Lin, B. Yang, Q. Wang, H. Pan, Z. Cai, H. Li, M. Cao, J. Hu, Y.-R. Lu, T.-S. Chan, E. Cortes, A. Fratalocchi and M. Liu, *Nano Energy*, 2021, **82**, 105767.

55 X. F. Lu, L. Yu and X. W. Lou, *Sci. Adv.*, 2019, **5**, eaav6009.

This journal is © The Royal Society of Chemistry 2024

J. Mater. Chem. A, 2024, **12**, 4484–4491 | **4491**